RSC Advances

PAPER

View Article Online
View Journal | View Issue



Cite this: *RSC Adv.*, 2019, **9**, 3550

# $CrO_2$-based heterostructure and magnetic tunnel junction: perfect spin filtering effect, spin diode effect and high tunnel magnetoresistance

Jiangchao Han,[a] Jimei Shen[b] and Guoying Gao *[ac]

Received 30th September 2018
Accepted 17th January 2019

DOI: 10.1039/c8ra08107g

rsc.li/rsc-advances

Half-metallic ferromagnetic $CrO_2$ has attracted much interest due to its 100% spin polarization and high Curie temperature. $CrO_2$ films have been fabricated on a $TiO_2$ (100) substrate. However, there have been no reports on the spin transport properties of devices based on a $CrO_2$ electrode and $TiO_2$ barrier. In this work, we use first-principles calculations combined with a nonequilibrium Green's function method to investigate the bias-voltage-dependent spin transport properties for the $CrO_2/TiO_2$ (100) heterostructure and the $CrO_2/TiO_2/CrO_2$ (100) magnetic tunnel junction (MTJ). Our results reveal the excellent spin filtering effect and spin diode effect in the heterostructure as well as the high tunnel magnetoresistance ratio (up to $4.48 \times 10^{14}$%) in the MTJ, which indicate potential spintronic applications. The origins of these perfect spin transport characteristics are discussed in terms of the calculated spin-dependent electrode band structures, the spin-dependent transmission spectra and semiconductor theory.



## 1. Introduction

Spintronic devices, which use electronic spin or both electronic charge and spin to increase the data processing speed and decrease electric power consumption compared to conventional semiconductor devices, have attracted more and more research interest.[1] One of the keys to high-performance spintronic devices is high spin injection efficiency from a magnetic material to a semiconductor, and thus high-spin-polarized materials are desired.[2] Half-metallic magnets,[3] which possess 100% spin polarization of electrons due to the fact that one of the two spin channels is metallic and the other has semiconductor or insulator characteristics, have been seen as promising candidates for high-spin-polarized materials and received extensive experimental and theoretical attention.[4–8]

Rutile $CrO_2$ is one of the most famous spintronic materials due to its nearly 100% spin polarization and high Curie temperature (394 K).[9–12] Rutile $TiO_2$ is a semiconductor with the same crystal structure and comparable lattice constant with $CrO_2$.[13] So, $TiO_2$ was usually used as the substrate to grow the $CrO_2$ films. Bulk half-metallic ferromagnetic $CrO_2$ is a metastable oxide phase that degrades at a high temperature (above 400 K) and atmospheric pressure into the thermodynamically more stable antiferromagnetic insulator $Cr_2O_3$ phase,[14] and there are more or less $Cr_2O_3$ at the surface of $CrO_2$,[15–17] however, with the improvement of experimental technology and the control of growth condition, single crystal $CrO_2$ films with a better crystalline quality and different orientations have been successfully grown on the $TiO_2$ (100), $TiO_2$ (001) and $TiO_2$ (110) substrates by the chemical vapor deposition technique.[17–20]

For the spintronic applications, there have been some studies on electronic transport properties based on $CrO_2$ electrode.[21–26] Meena and Choudhary[21–25] systemically investigated the spin transport properties for some magnetic tunnel junctions (MTJs) based on $CrO_2$ electrode and different barriers such as the graphene and the carbon nanotube, and large tunneling magnetoresistance (TMR) ratios were predicted. Leo *et al.*[26] experimentally studied the TMR in the MTJ of $CrO_2$/MgO/CoFe (100), and revealed that the TMR sign can be reversed simply by subtle modifications to the $CrO_2$/MgO interface. In addition, some MTJs, where $TiO_2$ as the barrier and other magnetic materials instead of $CrO_2$ as the electrodes, have also been explored.[27–30] These studies indicated that the large TMR ratio is related to the electrode with high spin polarization and the property of tunnel barrier in the MTJ. As far as we know, however, there is no report on the spin transport properties of the MTJ of $CrO_2/TiO_2/CrO_2$, considering the facile growth of the $CrO_2$ films on the $TiO_2$ (100) substrate,[17,20] it is meaningful to explore the potential spintronic applications for the $CrO_2/TiO_2$ (100) heterostructure and the $CrO_2/TiO_2/CrO_2$ (100) MTJ. In the present work, our calculations based on the first-principles combined with the nonequilibrium Green's function method reveal that the $CrO_2/TiO_2$ (100) heterostructure behaves obvious spin diode effect and spin filtering effect, and the $CrO_2/TiO_2/CrO_2$ (100) MTJ has a high TMR ratio (up to $4.48 \times 10^{14}$%).

[a]School of Physics, Huazhong University of Science and Technology, Wuhan 430074, China. E-mail: guoying_gao@mail.hust.edu.cn

[b]Nanjing Normal University Taizhou College, Taizhou 225300, China

[c]Wuhan National High Magnetic Field Center, Huazhong University of Science and Technology, Wuhan 430074, China

These results could be helpful for the experimental realization of $CrO_2$-based spintronic devices.

## 2. Computational details

Rutile $CrO_2$ belongs to the tetragonal structure ($P4_2/mnm$) with lattice parameters $a = b = 4.421$ Å and $c = 2.916$ Å,[31] while isostructural $TiO_2$ has the lattice parameters $a = b = 4.594$ Å and $c = 2.958$ Å.[32] Considering the experimental growth of $CrO_2$ (100) films on the $TiO_2$ (100) substrates and the small lattice mismatch along (100) direction (1.72%), we construct the $CrO_2$/$TiO_2$ (100) heterostructure and the $CrO_2$/$TiO_2$/$CrO_2$ (100) MTJ based on the $TiO_2$ lattice constant. As shown in Fig. 1, both models of the two devices are divided into three parts: the left electrode, the scattering region, and the right electrode. Note that there are four possible contacts for the interface between $CrO_2$ and $TiO_2$:Cr–O interface (type-I), Cr–Ti interface (type-II), O–Ti interface (type-III) and O–O interface (type-IV). We relax the four interfaces and the calculated total energies are −8752.1461, −8750.3011, −8751.7887 and −8749.9607 eV per cell for the four interfaces, respectively, which indicate that the type-I configuration is most stable relatively. So, in our present work, we focus on the type-I structure for the transport properties of the heterostructure and the MTJ.

Our calculations are performed by the Atomistix ToolKit (ATK) package, which combines the nonequilibrium Green's function (NEGF) and the density functional theory (DFT).[33,34] The generalized gradient approximation (GGA) with the Perdew–Burke–Ernzerhof (PBE) form is adopted for the electronic exchange–correlation functional.[35] Before calculating the transport properties, the interface relaxation is carried out until the force on each atom is less 0.01 eV $Å^{-1}$. The electron wave function of the linear combination of atomic orbitals (LCAO) is cut off at a kinetic energy of 2041 eV, and the Brillouin zone of the unit cell is sampled by using a $6 \times 4 \times 1$ $k$-point grid. In the calculations of transport properties, the Monkhorst–Pack $k$-meshes of both devices are $6 \times 4 \times 100$, the integration grid of the current calculation is $10 \times 10$, and the self-consistent calculations are limited to $2.7 \times 10^{-4}$ eV tolerance. All these parameters are tested to be sufficient to obtain accurate results, and the present method has been successfully used in our previous works on spin transport properties of magnetic heterostructures and MTJs.[36,37] The spin-dependent current is calculated by the Landauer-Buttiker formula:

$$I^{\uparrow(\downarrow)} = \frac{e}{h}\int_{-\infty}^{\infty}\{T^{\uparrow(\downarrow)}(E, V_b)[f_L(E-\mu_L) - f_R(E-\mu_R)]\}dE, \quad (1)$$

where $f_{L/R}(E - \mu_{L/R})$ is the Fermi–Dirac distribution for the left (right) electrode, and $\mu_{L/R} = E_F \pm eV/2$ is the corresponding electrochemical potential. $T^{\uparrow(\downarrow)}(E,V_b)$ is the spin-dependent transmission coefficient,

$$T^{\uparrow(\downarrow)}(E,V_b) = \mathrm{Tr}[\Gamma_L G^R \Gamma_R G^A]^{\uparrow(\downarrow)}, \quad (2)$$

where $G^{R(A)}$ is the retarded (advanced) Green's function of the central region, and $\Gamma_{L(R)}$ is the coupling matrix of the left (right) electrode.

## 3. Results and discussion

### 3.1. Spin diode and spin filtering effects in the $CrO_2$/$TiO_2$ heterostructure

We first study the spin transport properties of the $CrO_2$/$TiO_2$ (100) heterostructure. The spin-resolved current is calculated under the bias voltage range from −1 V to 1 V, as shown in Fig. 2. It is clear that the spin-down current is absolutely inhibited. For the spin-up current, the value is close to zero when the applied voltage is positive. When the negative voltage is applied, however, the spin-up current rapidly increases with the increasing negative bias voltage. Hence the heterostructure exhibits perfect spin diode effect in the spin-up channel and successfully filters out the spin-down current. The rectification ratio,[38] $RR(V) = |I(-V)/I(V)|$, is usually used to evaluate the diode performance, and a large rectification ratio means a good diode effect. Fig. 2 indicates that the largest RR value in the spin-up channel reaches $7.8 \times 10^5$ at 0.75 V. Such a large RR indicates excellent unidirectional conductivity, making $CrO_2$ a promising candidate for spin diode application. In addition, we calculate the efficient of the spin filtering by $\eta = [(I_\uparrow - I_\downarrow)/(I_\uparrow + I_\downarrow)] \times 100\%$, where $I_\uparrow$ and $I_\downarrow$ are the spin-up and spin-down currents, respectively.[39] As shown in Fig. 2(b), the efficiency of the spin filtering is almost complete.

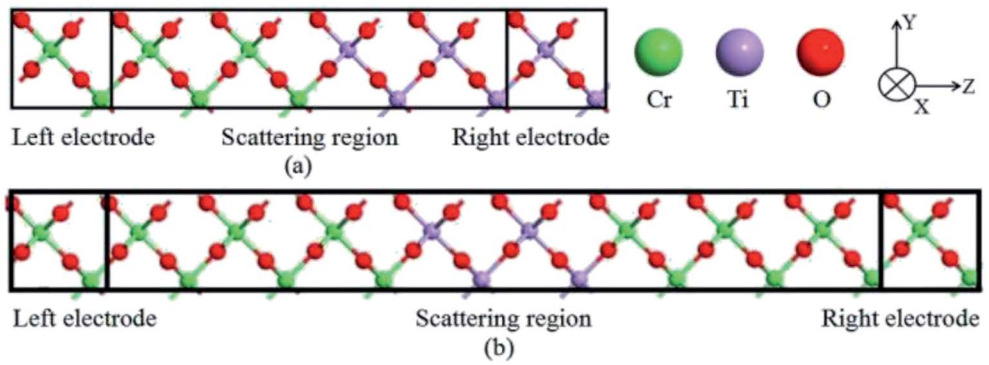


Fig. 1 Schematic illustrations of the devices of the $CrO_2$/$TiO_2$ (100) heterostructure (a) and the $CrO_2$/$TiO_2$/$CrO_2$ (100) magnetic tunnel junction (MTJ) (b). The $z$ direction is the transmission direction.

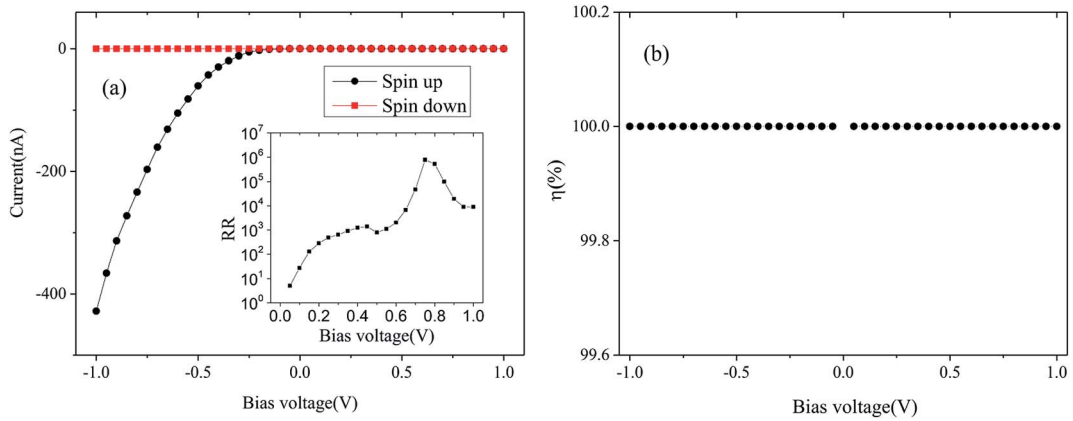


Fig. 2 (a) The spin-dependent current-bias voltage curve of the $CrO_2/TiO_2$ (100) heterostructure. The inset is the rectification ratio (RR) in spin-up channel with the change of bias voltage. (b) The spin-filtering efficiency $\eta$ (in %) *versus* bias voltage.

We further present in Fig. 3 the calculated spin-dependent band structures of the left electrode $CrO_2$ (100) and the right electrode $TiO_2$ (100) in order to explain the spin-dependent current–voltage curve. One can see from Fig. 3 that the left electrode $CrO_2$ is a typical half-metal: a metallic characteristic in the spin-up channel and the Fermi-level falls in a large energy gap in the spin-down channel. The top of the spin-down valence bands is about 0.91 eV below the Fermi level at the (000) $k$ point, and the bottom of the spin-down conduction bands is about 3.64 eV above the Fermi level at the same $k$ point. For the right electrode $TiO_2$ (100), the top of the valence bands is tangent to the Fermi level and there is a wide band gap above the Fermi level. According to the electrochemical potentials of the left and right electrodes, $\mu_{L/R} = E_F \pm (1/2)eV_b$, the Fermi level of the left electrode (right electrode) will move down (up) $(1/2)eV_b$ when a positive bias voltage $V_b$ is applied. Therefore, in the applied voltage range from 0 V to 1 V, the spin-up valence bands of the left electrode cross the Fermi level and the transmission channel is generated in the spin-up channel of the left electrode. At the same time, the Fermi level of the right electrode falls in the semiconductor gap. Such a big gap could not motivate the right electrode to produce transmission channel. Hence, either in the spin-up or spin-down state, the Bloch states of the left electrode are unable to go through the right electrode at a positive bias voltage, because there is no transmission channel to receive them. So, the forward current in both spin channels is zero at the positive bias voltage range. However, when the negative bias voltage is applied to the device, the spin-up conduction bands of the left electrode cross the Fermi level, and thus some transmission channels are generated.

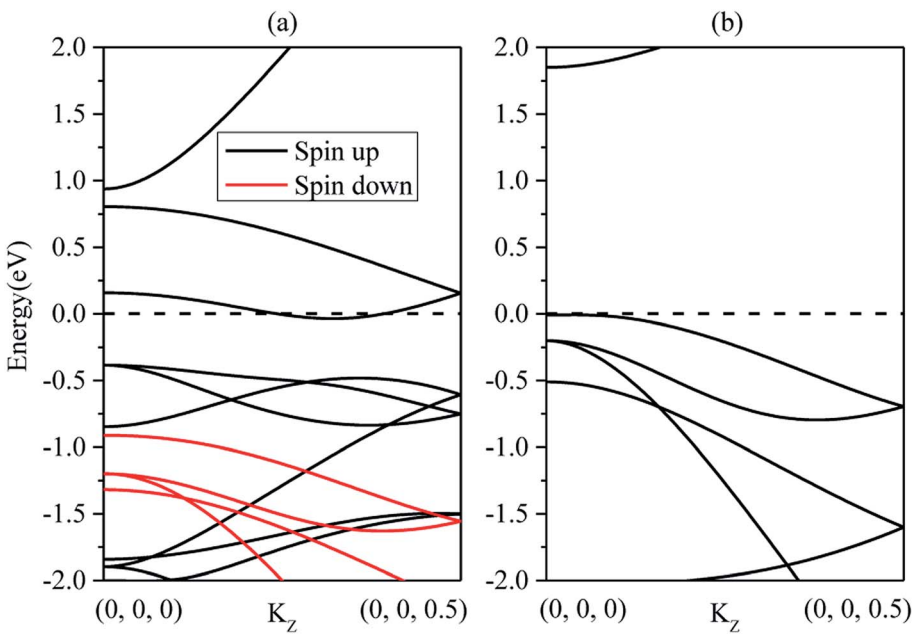


Fig. 3 Band structures along the (100) direction for the left electrode $CrO_2$ (a) and the right electrode $TiO_2$ (b). The dashed line means the Fermi level at zero eV.

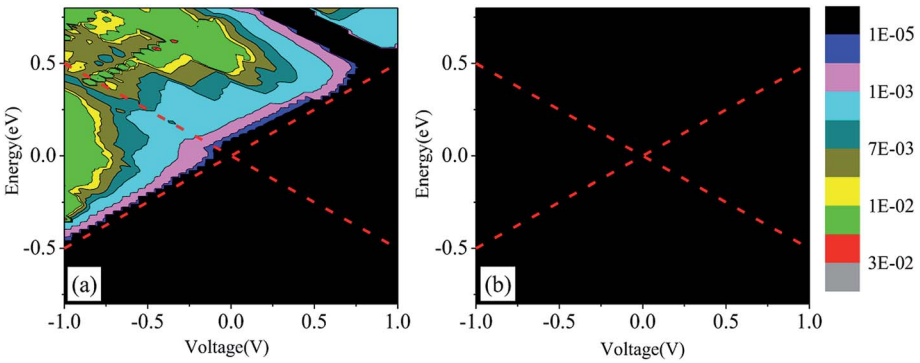


Fig. 4 The spin-dependent transmission spectra in the spin-up (a) and spin-down (b) channels for the $CrO_2/TiO_2$ (100) heterostructure.

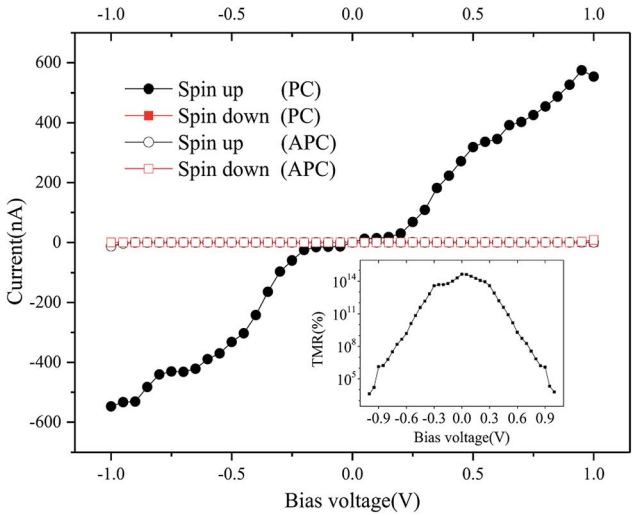


Fig. 5 The spin-dependent current-bias voltage curve of the $CrO_2/TiO_2/CrO_2$ (100) MTJ in the PC and the APC. The inset shows the TMR with the change of bias voltage.

Meanwhile, the Fermi level of the right electrode moves down, and in turn, the valence bands of right electrode cross the Fermi level, producing transmission channels. The well match of the spin-up resonance channels of two electrodes provides the transmission condition. This is similar to the open-circuit state. With the increase of the negative bias voltage, more and more bands cross the Fermi level, resulting in the increase of the transmission channels and the spin-up current, and thus the diode effect emergences in the spin-up channel. In the bias voltage range, the spin-down bands of $CrO_2$ are never able to cross the Fermi level due to the relatively wide band gaps above and below the Fermi level in the spin-down channel of the $CrO_2$ electrode. Therefore, there is no Bloch state in the spin-down channel and the spin-down current is zero, resulting in the spin filtering effect at the negative bias voltage.

To further understand the mechanism of the spin diode effect and the spin filtering effect, we show in Fig. 4 the calculated bias voltage-dependent transmission spectra. The red dotted lines represent the electrochemical potentials of the left/right electrode, and the area between lines denotes the bias window. Note that the spin-polarized current can be obtained through the energy integral of transmission coefficients over the bias window. For the spin-up transmission spectra (Fig. 4(a)), there is no transmission coefficient in the positive bias window. So, the spin-up current is zero at the positive bias voltage. However, different phenomenon appears in the negative bias window, *i.e.*, with the increase of the negative bias voltage, the transmission coefficient value becomes more and more large, and the area of bias window becomes broader and broader. So, the spin-up current increases with increasing negative bias voltage, *i.e.*, the diode effect appears in the spin-up channel. However, for the spin-down transmission spectra (Fig. 4(b)), neither negative nor positive bias window is filled with transmission coefficient. So, the spin-down current is inhibited, leading to the spin filtering effect in the negative bias voltage range.

### 3.2. High tunnel magnetoresistance in the $CrO_2/TiO_2/CrO_2$ magnetic tunnel junction

We now calculate the spin transport properties of the $CrO_2/TiO_2/CrO_2$ (100) MTJ. The parallel magnetization configuration (PC) and the antiparallel magnetization configuration (APC) between the left and right $CrO_2$ electrodes are considered. Fig. 5 shows the calculated spin-dependent current with the change of bias voltage in the PC and APC. One can see clearly from Fig. 5 that the spin-down current in the PC and both spin-up and spin-down currents in the APC are almost zero in the bias voltage range considered. Only the spin-up current in the PC is considerable and it rapidly increases with increasing bias voltage. These distinctive *I–V* characteristics lead to the large TMR ratio, as shown in the inset of Fig. 5, it reaches $4.48 \times 10^{14}$% at zero bias voltage. Note that, there are usually three definitions of the TMR value: the "optimistic", the "pessimistic" and the "normalized" TMR.[40] Here, we adopt the optimistic TMR $= [(I_P - I_{AP})/I_{AP}] \times 100\%$, where $I_P$ ($I_{AP}$) is the total (spin-up plus spin-down) current for the MTJ in the PC (APC).[40] To explain the I–V characteristics and the large TMR ratio, we calculate the spin-dependent band structures of the $CrO_2$ electrode in the PC and APC (Fig. 6). For the PC, the magnetization directions of two electrodes are same, and thus the band structure of the left electrode (Fig. 6(a)) is identical to that of the

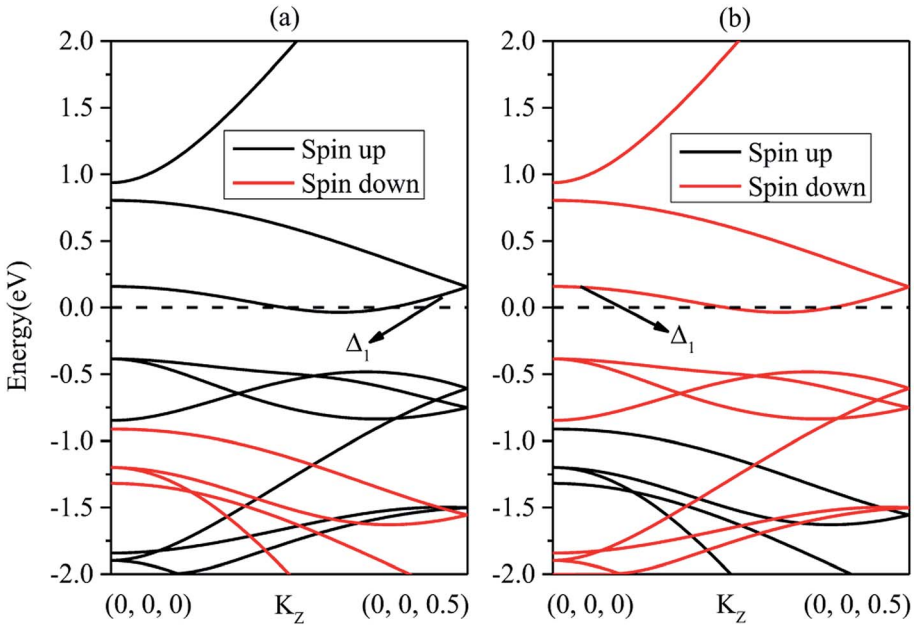


Fig. 6 Band structures along the (100) direction for the left and right electrodes of the $CrO_2/TiO_2/CrO_2$ (100) MTJ in the PC [(a) and (a)] and the APC [(a) and (b)].

right electrode (Fig. 6(a)). When a positive bias voltage is applied to the MTJ, the Fermi level of the left electrode moves down, and the Fermi level of the right electrode moves up. Due to the metallic properties in the spin-up direction, the Fermi levels of two electrodes always cross the bands and the transmission channels are generated in the spin-up channel of two electrodes simultaneously. So, the Bloch states started in the left electrode can be well received in the right electrode. With the increase of applied bias voltage, the spin-up current is increased. The same situation also appears in the case of the negative bias voltage. At the same time, we also note the semiconductor characteristic with a large energy gap in the spin-down channel. No matter what the bias voltage is applied in the PC, the large band gap always prevents the generation of transmission channels in the spin-down channel, and thus there is no spin-down current in the PC.

For the APC, the magnetization directions of two electrodes are completely opposite. That is, the spin-up bands and the spin-down bands are exchanged between the two electrodes. So, the band structures of the left and right electrodes correspond to Fig. 6(a) and (b), respectively. This spin-dependent inverse band structures between two electrodes and the large energy gap in one of the two spin channels result in the mismatch of the transmission channels no matter a positive or a negative bias voltage is applied, and in turn, both the spin-up and spin-down currents in the APC are suppressed. Therefore, the negligible current in the APC make the TMR ratio large. In order to explain the largest TMR value at the zero bias voltage (Fig. 5), we list in Table 1 the typical transport properties of the $CrO_2/TiO_2/CrO_2$ (100) MTJ. For the spin-up channel in the PC, the maximum transmission coefficient reaches 0.184, which is relatively larger in transport. It is to say, the incoming wave function of the left electrode $\Delta_1$ band (Fig. 6) is slightly scattered and the right electrode receives most of the incoming wave. For the spin-down channel in the PC, the transmission coefficient is much smaller than that in the spin-up channel, because the incoming wave function of $\Delta_1$ band is nearly nonexistent. According to the definition of spin polarization, $SP = [(G_\uparrow - G_\downarrow)/(G_\uparrow + G_\downarrow)] \times 100\%$, where $G_\uparrow$ and $G_\downarrow$ are the spin-up and spin-down conductions, respectively. The calculated spin polarization in the PC reaches 100%. This indicates that the $CrO_2$ electrode is a good spin injection source for the device. For the spin-up and spin-down channels in the APC, the maximum transmission coefficients are very small, because the incoming wave function of $\Delta_1$ band only appears in one spin channel, and there is no corresponding $\Delta_1$ symmetry state to receive them. Therefore, the incoming wave always decays along the transport direction, and both spin-up and spin-down conductions in the APC are very small. The great differences of $T_{MAX}$ and $G$ between the PC and APC at zero bias voltage result in the huge TMR ratio.

It should be pointed out that the TMR value is usually dependent on the thickness of the barrier, so we further calculate the $TiO_2$ layers dependence of TMR ratio, as shown in Fig. 7. It shows that the TMR value oscillates with the increase of

Table 1 Calculated spin transport properties of the $CrO_2/TiO_2/CrO_2$ (100) MTJ in the parallel magnetization configuration (PC) and the antiparallel magnetization configuration (APC). $T_{MAX}$ is the largest transmission coefficient, $G$ is the quantum conduction, and SP is the spin polarization at zero bias voltage for the MTJ

| | $T_{MAX}$ | $G$ (siemens) | SP (%) |
|---|---|---|---|
| Spin-up in PC | $1.84 \times 10^{-1}$ | $3.68 \times 10^{-7}$ | 100.00% |
| Spin-down in PC | $2.03 \times 10^{-16}$ | $1.95 \times 10^{-22}$ | |
| Spin-up in APC | $4.04 \times 10^{-14}$ | $8.22 \times 10^{-20}$ | 99.99% |
| Spin-down in APC | $3.67 \times 10^{-18}$ | $4.72 \times 10^{-24}$ | |

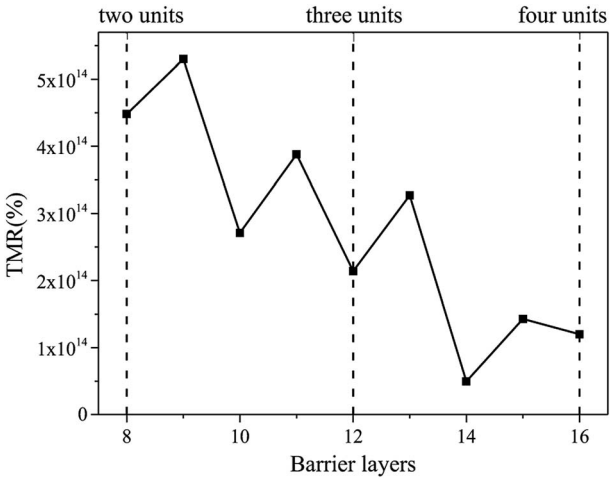


Fig. 7 The $TiO_2$ barrier thickness dependence of the TMR ratio in the $CrO_2/TiO_2/CrO_2$ (100) MTJ. The three dashed lines represent the thickness of two, three and four $TiO_2$ units, respectively.

the barrier thickness, but it still reaches $\sim 10^{14}$% when the thickness of the barrier is increased to three or four $TiO_2$ units. According to the Julliere model, TMR ratio is determined by spin polarization of both electrodes and irrelevant to barrier thickness.[41] The TMR oscillatory indicates that the coherency of electron wave functions is conserved across the barrier, and $TiO_2$ plays a selective filtration role in transport mechanism.

Finally, we use the semiconductor theory to explain the current change with bias voltage in different magnetization configurations of the $CrO_2/TiO_2/CrO_2$ (100) MTJ. Fig. 8 indicates the calculated spin-dependent device density of states (DDOS). When the applied voltage is zero in the PC, the Fermi levels of left and right electrodes are located at the same energy level, as shown in Fig. 8(a) and (b). It is found that the device is a typical metal–semiconductor–metal (MSM)[42] structure in the spin-up channel, and the apparent metal induced gap states (MIGS) are formed at the region of $TiO_2$ due to the Fermi level pinning of semiconductor and metal.[43] During the pinging process, the Schottky barriers appear on the two metal–semiconductor interfaces. Under a positive bias voltage such as 0.5 V [Fig. 8(c)], the Fermi level of the left electrode shifts down, leading to the decrease of the barrier height around the left interface of the device. A lot of holes coming from the left electrode begin to inject into the $TiO_2$ intrinsic semiconductor. The rising Fermi level of the right electrode makes electrons inject into $TiO_2$ barrier from right to left. $TiO_2$ stores a lot of electrons and holes, and these carriers recombination causes $TiO_2$ resistivity to be lower. So, the higher the bias voltage between two electrodes, the bigger the passing spin-up current in the MSM structure. For the spin-down channel of the PC (Fig. 8(b) and (d)), the device is made of three wide band gap semiconductors. There is no carrier within bias window under a positive bias voltage. So, the high insulation resistance device generates negligible current. Fig. 8(e)–(h) are the spin-dependent DDOS in the APC under the bias voltages of zero and 0.5 V. In both spin-up and spin-down states, the devices are composed of the insulator–semiconductor–metal structure or the metal–semiconductor–insulator structure, which are similar to the metal–insulator–semiconductor (MIS) structure.[44] MIS plays the role of capacitor in the circuit and the electric conductive performance is poor, because there is no charge in the insulator region. So, the currents at positive bias voltage in the APC are very small and negligible, and this similar phenomenon is also found at the negative bias voltage in the APC (not shown here).

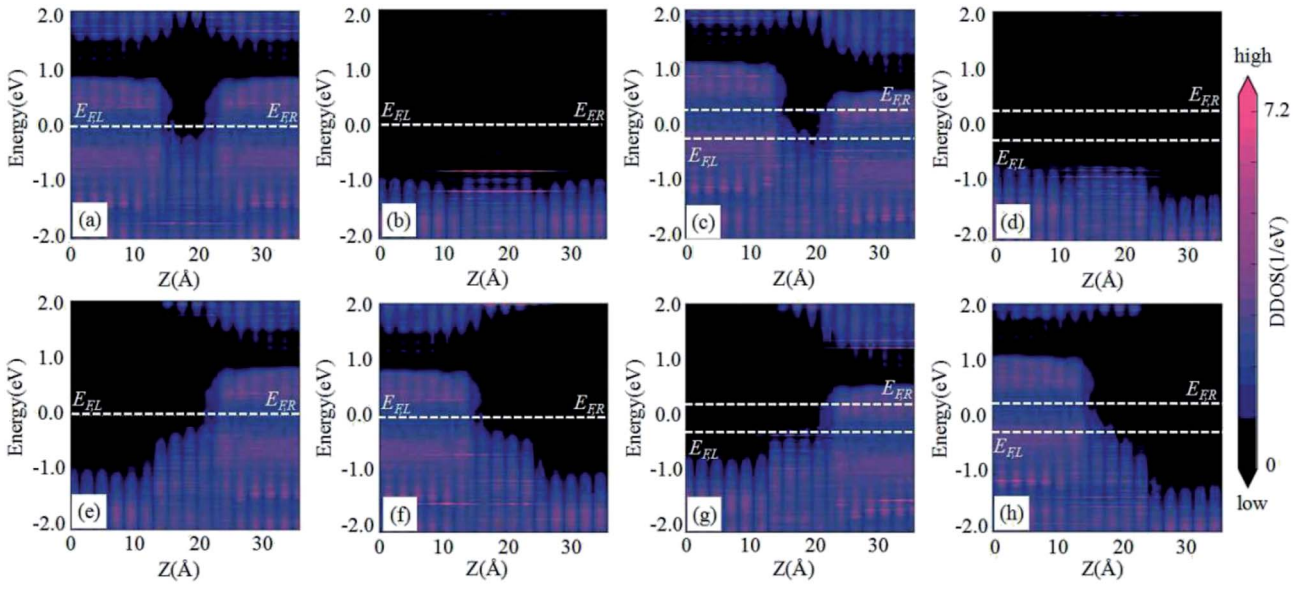


Fig. 8 The spin-dependent device density of states (DDOS) for the $CrO_2/TiO_2/CrO_2$ (100) MTJ at the bias voltages of zero V in the PC [(a) and (b)], 0.5 V in the PC [(c) and (d)], zero V in the APC [(e) and (f)] and 0.5 V in the APC [(g) and (h)]. [(a), (c), (e) and (g)] and [(b), (d), (f) and (h)] represent the spin-up and spin-down channels, respectively.

## 4. Conclusion

Half-metallic $CrO_2$ with 100% spin polarization make it meaningful to study the spin transport properties of the spintronic devices based on the $CrO_2$ electrode. Motivated by the experimental growth of the $CrO_2$ (100) films on $TiO_2$ (100) substrate, we construct the spintronic devices of the $CrO_2/TiO_2$ (100) heterostructure and the $CrO_2/TiO_2/CrO_2$ (100) MTJ. By using the first-principles calculations combined with the nonequilibrium Green's function, we predict the excellent spin diode and spin filtering effects in the heterostructure as well as the high TMR ratio in the MTJ, which indicate the potential spintronic applications of $CrO_2$. We also discuss the formation mechanism of these perfect spin transport properties from the calculated spin-dependent electrode band structures, the transmission spectra and the device density of states.

## Conflicts of interest

There are no conflicts to declare.

## Acknowledgements

This work was supported by the National Natural Science Foundation of China under Grant No. 11474113 and No. 11504278.

## References

1 A. Hirohata and K. Takanashi, *J. Phys. D: Appl. Phys.*, 2014, **47**, 193001.
2 G. Schmidt, D. Ferrand, L. W. Molenkamp, A. T. Filip and B. J. van Wees, *Phys. Rev. B: Condens. Matter Mater. Phys.*, 2000, **62**, R4790–R4793.
3 R. A. de Groot, F. M. Mueller, P. G. V. Engen and K. H. J. Buschow, *Phys. Rev. Lett.*, 1983, **50**, 2024–2027.
4 H. C. Kandpal, G. H. Gerhard and C. Felser, *J. Phys. D: Appl. Phys.*, 2007, **40**, 1507–1523.
5 X. Wu, J. Han, Y. Feng, G. Li, C. Wang, G. Ding and G. Gao, *RSC Adv.*, 2017, **7**, 44499–44504.
6 J. He, P. Lyu and P. Nachtigall, *J. Mater. Chem. C*, 2016, **4**, 11143–11149.
7 R. Hu, Z. H. Zhang and Z. Q. Fan, *Phys. Chem. Chem. Phys.*, 2017, **19**, 20137–20146.
8 M. M. Monshi, S. M. Aghaei and I. Calizo, *RSC Adv.*, 2016, **7**, 18900–18908.
9 K. Schwarz, *J. Phys. F: Met. Phys.*, 1986, **16**, L211.
10 Y. Ji, G. J. Strijkers, F. Y. Yang, C. L. Chien, J. M. Byers, A. Anguelouch, G. Xiao and A. Gupta, *Phys. Rev. Lett.*, 2001, **86**, 5585–5588.
11 A. Anguelouch, A. Gupta, G. Xiao, D. W. Abraham, Y. Ji, S. Ingvarsson and C. L. Chien, *Phys. Rev. B: Condens. Matter Mater. Phys.*, 2001, **64**, 180408(R).
12 T. J. Swoboda, P. Arthur, N. L. Cox, J. N. Ingraham, A. L. Oppegard and M. S. Sadler, *J. Appl. Phys.*, 1961, **32**, 374S–375S.
13 D. O. Scanlon, C. W. Dunnill, J. Buckeridge, S. A. Shevlin, A. J. Logsdail, S. M. Woodley, C. R. Catlow, M. J. Powell, R. G. Palgrave, I. P. Parkin, G. W. Watson, T. W. Keal, P. Sherwood, A. Walsh and A. A. Sokol, *Nat. Mater.*, 2013, **12**, 798–801.
14 L. W. Fringer and R. M. Hazen, *J. Appl. Phys.*, 1980, **51**, 5362.
15 R. Cheng, B. Xu, C. N. Borca, A. Sokolov, C. S. Yang, L. Yuan, S. H. Liou, B. Doudin and P. A. Dowben, *Appl. Phys. Lett.*, 2001, **79**, 3122.
16 J. Dho, D.-H. Kim, D. Kwon and B. G. Kim, *J. Appl. Phys.*, 2008, **104**, 063528.
17 H. Fujiwara, M. Sunagawa, K. Terashima, T. Kittaka, T. Wakita, Y. Muraoka and T. Yokoya, *Appl. Phys. Lett.*, 2015, **106**, 202404.
18 P. B. Visscher, P. R. LeClair and A. Gupta, *Appl. Phys. Lett.*, 2013, **102**, 162410.
19 K. B. Chetry, M. Pathak, P. LeClair and A. Gupta, *J. Appl. Phys.*, 2009, **105**, 083925.
20 M. Rabe, J. Pommer, K. Samm, B. Özyilmaz, C. König, M. Fraune, U. Rüdiger, G. Güntherodt, S. Senz and D. Hesse, *J. Phys.: Condens. Matter*, 2002, **14**, 7.
21 S. Meena and S. Choudhary, *Phys. Chem. Chem. Phys.*, 2017, **19**, 17765–17772.
22 S. Meena and S. Choudhary, *Phys. Lett. A*, 2017, **381**, 3431–3439.
23 S. Meena and S. Choudhary, *AIP Adv.*, 2017, **7**, 125008.
24 S. Meena and S. Choudhary, *Mater. Chem. Phys.*, 2018, **217**, 175–181.
25 A. K. Singh, S. Choudhary and S. Meena, *J. Supercond. Novel Magn.*, 2018, **31**, 2753–2758.
26 T. Leo, C. Kaiser, H. Yang, S. S. P. Parkin, M. Sperlich, G. Güntherodt and D. J. Smith, *Appl. Phys. Lett.*, 2007, **91**, 252506.
27 V. Garcia, M. Bibes, A. Barthélémy, M. Bowen, E. Jacquet, J. P. Contour and A. Fert, *Phys. Rev. B: Condens. Matter Mater. Phys.*, 2004, **69**, 052403.
28 K. M. Kim, B. J. Choi, M. H. Lee, G. H. Kim, S. J. Song, J. Y. Seok, J. H. Yoon, S. Han and C. S. Hwang, *Nanotechnology*, 2011, **22**, 254010.
29 M. Bibes, M. Bowen, A. Barthélémy, A. Anane, K. Bouzehouane, C. Carrétéro, E. Jacquet, J. P. Contour and O. Durand, *Appl. Phys. Lett.*, 2003, **82**, 3269–3271.
30 H. Mahmoudi, T. Windbacher, V. Sverdlov and S. Selberherr, *21st International Conference "MIXDES 2014"*, Lublin, Poland, 2014, June 19–21, pp. 58–61.
31 M. S. Anwar and J. Aarts, *Phys. Rev. B: Condens. Matter Mater. Phys.*, 2013, **88**, 085123.
32 J. K. Burdett, T. Hughbanks, G. J. Miller, J. W. Richardson Jr and J. V. Smith, *J. Am. Chem. Soc.*, 1987, **109**, 3639–3646.
33 J. Taylor, H. Guo and J. Wang, *Phys. Rev. B: Condens. Matter Mater. Phys.*, 2001, **63**, 245407.
34 M. Brandbyge, J.-L. Mozos, P. Ordejón, J. Taylor and K. Stokbro, *Phys. Rev. B: Condens. Matter Mater. Phys.*, 2002, **65**, 165401.
35 J. P. Perdew, K. Burke and M. Ernzerhof, *Phys. Rev. Lett.*, 1996, **77**, 3865.
36 G. Y. Gao and K. L. Yao, *Appl. Phys. Lett.*, 2014, **105**, 182405.

 

37 J. Li, G. Gao, Y. Min and K. Yao, *Phys. Chem. Chem. Phys.*, 2016, **18**, 28018–28023.
38 Z. Zhu, Z. H. Zhang, D. Wang, X. Q. Deng, Z. Q. Fan and G. P. Tang, *J. Mater. Chem. C*, 2015, **3**, 9657–9663.
39 J. Zeng and K. Q. Chen, *J. Mater. Chem. C*, 2015, **3**, 5697–5702.
40 X. Feng, O. Bengone, M. Alouani, I. Rungger and S. Sanvito, *Phys. Rev. B: Condens. Matter Mater. Phys.*, 2009, **79**, 214432.
41 M. Julliere, *Phys. Lett.*, 1975, **54A**, 225–226.
42 S. M. Sze, D. J. Coleman and A. Loya, *Solid-State Electron.*, 1971, **14**, 1209–1218.
43 V. Heine, *Phys. Rev.*, 1965, **138**, A1689.
44 P. Cova, A. Singh and R. A. Masut, *J. Appl. Phys.*, 1997, **82**, 5217.